INORGANIC CHEMISTRY
FRONTIERS

CHINESE CHEMICAL SOCIETY

ROYAL SOCIETY OF CHEMISTRY

RESEARCH ARTICLE

View Article Online
View Journal | View Issue

Published on 13 December 2023. Downloaded by Fail Open on 07/05/2025 8:52:43 AM.

Check for updates

Cite this: *Inorg. Chem. Front.*, 2024, **11**, 899

Carbon quantum dot regulated electrochemical activation of $Co_{0.03}Ni_{0.97}$LDH for energy storage†

Wenchao Chen,[a] Hongying Quan,*[a,b] Xiangyu Chen,[c] Hua Wang[c] and Dezhi Chen*[a]

Received 5th October 2023,
Accepted 9th December 2023

DOI: 10.1039/d3qi02027d

rsc.li/frontiers-inorganic

The valence and coordination structure of transition metals in electrode materials play a crucial role in the electrochemical energy storage process. However, it is still challenging to modulate the chemical environment of transition metals in multi-metal-based electrode materials because of the presence of charge exchange between the different metal ions. Here, a bimetallic-based electrode material, $Co_{0.03}Ni_{0.97}$LDH, with low electrochemical activity is transformed into a highly active one through a simple and efficient electrochemical activation process with the assistance of carbon quantum dots (CQDs). It reveals that CQDs can provide a fast charge transfer channel for the unique valence regulation between Co and Ni, resulting in the generation of high concentrations of Co^{3+} and Ni^{2+}, which is beneficial for upgrading the energy density of the electrode material and mitigating the Jahn–Teller distortion during the conversion of Ni^{2+}/Ni^{3+}. Moreover, the distinctive 5-coordination structures of Co can effectively stabilize the active sites of both Ni^{2+} and Co^{3+}. The activated CQD-modified $Co_{0.03}Ni_{0.97}$LDH composites (A-CQD/$Co_{0.03}Ni_{0.97}$LDH) deliver a high specific capacity of 2408 F g^{-1} at 1 A g^{-1} and maintain a high capacity retention of 90% after 2000 cycles at 10 A g^{-1}. The assembled asymmetric supercapacitor and the aqueous Ni–Zn battery show a high energy storage density of 0.25 mW h cm^{-2} at a power density of 2.25 mW cm^{-2} and 1.44 mW h cm^{-2} at 0.72 mW cm^{-2}, respectively. The impressive results provide a feasible strategy for the rational design of multi-metal-based electrode materials.

Introduction

An urgent need exists for developing a high-performance electrochemical energy storage device to solve the energy crisis and environmental problems as the demand for energy is increasing.[1–3] Electrode materials play a crucial role in the design of electrochemical energy storage devices. The development of high-performance electrode materials has become a major research focus for materials scientists and technicians.[4–6] Among the many electrode materials available, transition metal hydroxides ($M(OH)_y$, M = Fe, Co, Ni, *etc.*) are excellent battery-type electrode materials due to their abundant redox reactive sites and high theoretical capacity.[7–9] However, the slow ion transport and electron transfer dynamics of transition metal hydroxides during energy storage results in large internal resistance and poor rate performance.[10] In addition, the volume change during ion embedding and the Jahn–Teller distortion cause crystal structure distortion in the electrode material, leading to poor cycling stability.[11,12] These problems are serious obstacles to the further application of $M(OH)_y$ in energy storage. To overcome these inherent limitations, there is an urgent need for a simple and effective strategy to enhance the electrochemical performance of $M(OH)_y$ for next generation energy storage devices.

Electrochemical activation technology, also referred to as electrochemical reconstruction or electrochemical conversion, is a simple and efficient approach to improve the electrochemical performance of electrode materials.[13] After the process of electrochemical activation, materials with poor electrochemical properties, even inert materials, could be converted into highly active materials to significantly increase their energy storage capacity.[14] *In situ* or *ex situ* measurements revealed that electrochemical activation is primarily achieved by modulating the microstructure[15] and/or elemental composition of the electrode material[16] with the aim of increasing

---

[a] *Key Laboratory of Jiangxi Province for Persistent Pollutants Control and Resources Recycle, School of Environmental and Chemical Engineering, Nanchang Hangkong University, Nanchang 330063, China. E-mail: quanhongying@nchu.edu.cn, chendz@nchu.edu.cn*

[b] *School of Materials Science and Engineering, Nanchang Hangkong University, Nanchang 330063, China*

[c] *School of Chemistry, Key Laboratory of Bio-Inspired Smart Interfacial Science and Technology of Ministry of Education, Beihang University, 100191 Beijing, China*

† Electronic supplementary information (ESI) available. See DOI: **https://doi.org/10.1039/d3qi02027d**

Published on 13 December 2023. Downloaded by Fail Open on 07/05/2025 8:52:43 AM.

their energy storage capabilities. So far, transition metal hydroxides,[17] phosphides,[18] sulphides,[19] and nitrides[20] have been employed extensively as electrochemical activation materials. Among them, cobalt/nickel double hydroxide (CoNiLDH), a typical electrochemically activated material, has been extensively investigated for its electrochemical activation mechanisms.[21] During the electrochemical activation, the transformation of the morphology[22] and dynamic changes[16] in the content between Ni^{2+} and Ni^{3+}, Co^{2+} and Co^{3+} are the critical factors affecting the energy storage performance of CoNiLDH. The previous work[23] reported that the increased Co^{3+} content *via* electrochemical activation could improve the electrochemical performance of CoNiLDH. Meanwhile, the low-spin Co^{3+} can provide a positive contribution to diminish the structural distortions induced by high-spin Ni^{3+}.[24] According to the redox reaction of CoNiLDH, Ni^{2+} is the main active species for charge storage.[25] However, Co^{3+} with stronger oxidation can oxidize Ni^{2+} to Ni^{3+}, resulting in the reduction of energy storage capacity. Eventually, the two high-spin sites of Ni^{3+} and Co^{2+} would induce the structural collapse of CoNiLDH because of the Jahn–Teller distortion during the energy storage process. To date, most of the studies have highlighted the dominance of Co^{3+} at the expense of the effect of Ni^{3+} on the electrochemical properties of CoNiLDH. Therefore, the generated Ni^{3+} from the oxidation of Ni^{2+} by Co^{3+} during the electrochemical activation of CoNiLDH needs to be further investigated.

In the electrochemical activation process, the introduction of appropriate heteroatoms into the structure[26,27] or compositing with other active substances[28] in advance usually takes place with a view to improving the effect of electrochemical activation. Compared with pure CoNiLDH, the modified materials exhibited a rougher surface structure and more defects after electrochemical activation, which effectively shortens the electron and ion transfer pathways, thus accelerating the reaction kinetics. As a typical zero-dimensional carbon material, carbon quantum dots (CQDs) have received widespread attention in electrode materials in recent years due to their unique electronic properties and the capability of carrying various elements on their surface.[29,30] The reported literature suggested that the introduction of CQDs could not only optimize the microstructure of CoNiLDH to effectively accommodate the strain from the volume change during long-term cycling[31] but also create more defects in CoNiLDH to accelerate the reaction kinetics and improve the rate performance of the material.[32] To date, the information about the valence regulation between Ni and Co in CoNiLDH by CQDs is still lacking. In addition, the effect of highly reactive functional groups on the surface of CQDs on the coordination number of Ni and Co in the CoNiLDH structure has not yet been reported. Furthermore, the maintenance of a high content of both Ni^{2+} and Co^{3+} as the two active sites for energy storage in CoNiLDH by the regulation of the Ni and Co coordination environment needs to be further investigated.

Therefore, to reveal the effect of the dynamic changes of Co^{2+}/Co^{3+} on Ni^{2+}/Ni^{3+} and the mechanism of valence regulation of Co and Ni by CQDs during the electrochemical activation of CoNiLDH, herein, CQD/$Co_{0.03}Ni_{0.97}$LDH nanosheets were prepared by a one-step hydrothermal method using metal ion modified CQDs (M/CQDs, M = Co, Ni) and nickel nitrate as raw materials (see the ESI† for details). The metal ion-modified CQDs were obtained through the adsorption of Co^{2+} ions on S-doped CQDs. Further electrochemical activation using 200 cycles of cyclic voltammetry (CV) was carried out to prepare activated CQD/$Co_{0.03}Ni_{0.97}$LDH (abbreviated as A-CQD/$Co_{0.03}Ni_{0.97}$LDH). The XPS and XAFS results revealed that the excellent electron transport properties of CQDs enable the preferential oxidation of more Co^{2+} to the highly reactive Co^{3+} during electrochemical activation, while Ni^{3+} would be reduced to Ni^{2+} benefiting from the reductive nature of CQDs. EXAFS revealed the presence of Co–C/S bonds after electrochemical activation. Density functional theory (DFT) calculations showed that CQDs could regulate the charge distribution of $Co_{0.03}Ni_{0.97}$LDH, which solves the problem of difficult coexistence of high concentrations of Co^{3+} and Ni^{2+}, upgrading the capacity and relieving the Jahn–Teller distortion of $Co_{0.03}Ni_{0.97}$LDH. Moreover, A-CQD/$Co_{0.03}Ni_{0.97}$LDH exhibited a lower OH^- adsorption energy and redox reaction energy barrier than those of A-$Ni(OH)_2$ and A-$Co_{0.03}Ni_{0.97}$LDH. Consequently, A-CQD/$Co_{0.03}Ni_{0.97}$LDH delivered a high specific capacitance of 2408 F g^{-1} at 1 A g^{-1} in 6 M KOH, much greater than that of A-$Ni(OH)_2$ (1094 F g^{-1}) and A-$Co_{0.03}Ni_{0.97}$LDH (1026 F g^{-1}). Moreover, the assembled asymmetric supercapacitor could deliver a high energy storage density of 0.25 mW h cm^{-2} at a power density of 2.25 mW cm^{-2} and the assembled aqueous Ni–Zn battery could deliver a high energy storage density of 1.44 mW h cm^{-2} at a power density of 0.72 mW cm^{-2}. The above results provide a new understanding on the effect of CQDs on the enhanced electrochemical performance of bimetallic hydroxides.

Experimental

Materials

Carbon cloth (CC, WOS1002) was purchased from Taiwan Carbon Energy. $Zn(CH_3COO)_2$ (>99%), $Co(NO_3)_2 \cdot 6H_2O$ (>98.5%), $Ni(NO_3)_2 \cdot 6H_2O$ (>99.5%), KOH (>85.0%), citric acid (>99.5%), thiourea (>99%), urea (>99%), concentrated nitric acid (HNO_3, 65.0–68.0%), concentrated sulfuric acid (H_2SO_4, 98%), concentrated hydrochloric acid (HCl, 34–37%) and $KMnO_4$ (99%) were purchased from Shangtou Xilong Scientific. $Co(CH_3COO)_2 \cdot 4H_2O$ (>99.5%) and $Ni(CH_3COO)_2 \cdot 4H_2O$ (>99.0%) were acquired from Shanghai Macklin Biochemistry. All chemical reagents were used without further refinement.

Synthesis of S/CQDs

S/CQDs were prepared by a hydrothermal method reported in the previous work with minor modification.[33] 3 g of citric acid and 1.5 g of thiourea were completely dissolved in 30 mL of deionized water and stirred for 0.5 h at room temperature. The

Published on 13 December 2023. Downloaded by Fail Open on 07/05/2025 8:52:43 AM.

above mixture was then transferred to a 50 mL PTFE stainless steel autoclave and held at 200 °C for 10 hours. After the completion of the reaction, the autoclave was cooled naturally to room temperature. The resulting brownish yellow suspension was centrifuged at 8000 rpm for 30 min to remove large particles and the supernatant was collected to obtain the S/CQD solution.

Synthesis of M/CQDs

0.1 g of $M(NO_3)_2{\cdot}6H_2O$ (M = Co, Ni) was dissolved in 100 mL of deionized water and stirred for 0.5 h at room temperature. The above solution was then slowly added dropwise to 30 mL of S/CQD solution and stirred at room temperature for 1 hour. Then, the obtained precipitate of M/CQDs was collected by centrifugation and freeze-dried.

Synthesis of CQD/$Co_{0.03}Ni_{0.97}$LDH

0.1 g of Co/CQD powder was uniformly dispersed in 50 mL of deionized water. Then, 0.2488 g of $Ni(CH_3COO)_2{\cdot}4H_2O$ and 0.24 g of urea were dosed into the above dispersion. After stirring for 0.5 hours, the obtained reaction solution was transferred to a 100 ml PTFE-lined stainless-steel autoclave and held at 150 °C for 6 hours. After the completion of the reaction, the autoclave was cooled to room temperature naturally and the precipitate was collected and washed several times with distilled water and ethanol. The final product was freeze-dried and labelled as CQD/$Co_{0.03}Ni_{0.97}$LDH.

Synthesis of Co_xNi_{1-x}LDH

0.2438 g of $Ni(CH_3COO)_2{\cdot}4H_2O$, 0.0050 g of $Co(CH_3COO)_2{\cdot}4H_2O$ and 0.24 g of urea were completely dissolved in 50 mL of deionized water and stirred at room temperature for 0.5 h. The resulting reaction solution was transferred to a 100 mL PTFE-lined stainless-steel autoclave and held at 150 °C for 6 hours. The autoclave was cooled naturally to room temperature and the precipitate was then collected and washed several times with distilled water and ethanol. The final product was freeze-dried and labelled as $Co_{0.03}Ni_{0.97}$LDH. For comparison, the $Ni(OH)_2$, $Co_{0.2}Ni_{0.8}$LDH, $Co_{0.3}Ni_{0.7}$LDH, $Co_{0.4}Ni_{0.6}$LDH, $Co_{0.5}Ni_{0.5}$LDH, $Co_{0.7}Ni_{0.3}$LDH and $Co(OH)_2$ samples were also prepared using the above preparation process through changing the molar ratio of the Ni salt and Co salt.

Preparation of an activated carbon cloth (ACC) electrode

The plasma-treated CC was activated in a mixture of 20 mL of concentrated HNO_3, 40 mL of concentrated H_2SO_4, and 6 g of $KMnO_4$ for 24 h at 0 °C. The activated CC (ACC) was washed with deionized water and soaked in concentrated HCl for 12 h. Finally, the ACC was washed, dried, and used as the negative electrode.

Material characterization

The morphology and structure were observed using an FEI Quanta 250 scanning electron microscope (SEM) and an FEI Talos F200X transmission electron microscope (TEM). The phase was characterized on a Bruker D8 Advance XRD diffractometer (XRD) with Cu Kα radiation (λ = 1.5406 Å). The metal elements were determined using inductively coupled plasma mass spectrometry (ICP-MS, Thermo Fisher, iCAP RQ-MS). The elements and chemical states were analysed by Kratos Axis Ultra X-ray photoelectron spectroscopy (XPS). Fourier transform infrared spectroscopy (FTIR) was performed on a Bruker VERTEX70 FTIR spectrometer. The pore structure of the as-prepared samples was analysed using N_2 adsorption/desorption isotherms at 77 K obtained on a surface area & pore size analyser (Micromeritics TriStar II 3020). The XAFS tests were carried out at the Shanghai Synchrotron Radiation Centre facility, with Co or Ni K-edge absorption spectra in transmission mode and all XAFS spectra calibrated using Co or Ni foils. The EXAFS data were processed using the Athena module of the EXAFS software package and the quantitative curve was fitted using the Artemis module.[34]

Electrochemical measurements

The active material, conductive carbon black and polyvinylidene fluoride (PVDF) were mixed with *N*-methyl-2-pyrrolidone in a mass ratio of 8 : 1 : 1 to form a slurry. The resulting slurry was then coated onto a carbon cloth substrate of 1 cm × 1.5 cm (active area is 1 cm × 1 cm) after N_2-plasma treatment and dried at 60 °C for 12 hours. Electrochemical measurements were carried out on a Chenhua CHI760e electrochemical workstation using a three-electrode system in 6 M KOH aqueous solution at room temperature (25 ± 2 °C). Herein, the as-fabricated electrode, platinum plate (1 cm × 1 cm) and Hg/HgO electrode were used as the working electrode, the counter electrode, and the reference electrode, respectively. Cyclic voltammetry (CV), galvanostatic charge–discharge (GCD) analysis and electrochemical impedance spectroscopy (EIS) were performed to evaluate the electrochemical properties of the as-prepared electrodes. The mass capacity (C_m) of the as-prepared samples in the three-electrode system was calculated according to eqn (1), and the areal capacity (C_a) was calculated according to eqn (2), respectively.

$$C_{\mathrm{m}} = \frac{I\Delta t}{m\Delta V} \tag{1}$$

$$C_{\mathrm{a}} = \frac{I\Delta t}{S\Delta V} \tag{2}$$

where I, Δt, ΔV and m are the discharge current (A), discharge time (s), potential window (V) and mass loading of the active materials (g), and S is the area of the active substance of the electrode (cm^2).

In addition, an asymmetric supercapacitor device (ASC) was assembled using a piece of glass fiber filter paper as the separator, A-CQD/$Co_{0.03}Ni_{0.97}$LDH as the positive electrode, ACC as the negative electrode, and 6 M KOH as the electrolyte, respectively. The ACS was sealed with a PVC film, and its thickness was 1.7 mm. The electrochemical properties of the ASC were tested on a CHI760e electrochemical workstation and a CT2001A battery test system at room temperature (25 ± 2 °C).

Published on 13 December 2023. Downloaded by Fail Open on 07/05/2025 8:52:43 AM.

The energy density and power density of the ASC were calculated through the following eqn (3) and (4), respectively:

$$E_a = \frac{C_a(\Delta V)^2}{7.2} \tag{3}$$

$$P_a = \frac{3600 E_a}{\Delta t} \tag{4}$$

where ΔV (V) is the operating voltage range and Δt (s) is the discharge time.

The electrochemical performance of the assembled water-based Ni–Zn battery was tested using a two-electrode system. The CR2025 cells were assembled using a zinc flake and an as-prepared electrode as the anode and cathode, respectively. A solution of 0.2 M $Zn(CH_3COO)_2$ and 6 M KOH was used as the electrolyte and glass fiber filter paper was the separator. In addition, the mass loading of the active materials on the collect were about 3 mg cm^{-2} in the above three-electrode system, ACS and Ni–Zn battery.

Results and discussion

Characterization

The CV curves at the scan rate of 50 mV s^{-1} for the electrochemical activation process are shown in Fig. 1a–c. During the CV cycling, the intensity of the redox peaks and the area of the CV curve gradually increased, indicating that the specific capacity increased with CV cycling. It is evident that both $Ni(OH)_2$ and $Co_{0.03}Ni_{0.97}$LDH reached the electrochemical stability earlier in comparison with CQD/$Co_{0.03}Ni_{0.97}$LDH. The reconstruction of $Ni(OH)_2$ occurred mainly in the first 10 CV cycles, after which the capacity did not change obviously. Although $Co_{0.03}Ni_{0.97}$LDH eventually achieved excellent capacitive performance compared to $Ni(OH)_2$, it required longer activation time as well, becoming steady after 100 CV cycle activation. Likewise, CQD/$Co_{0.03}Ni_{0.97}$LDH involved longer activation times, and its capacity increased greater than that of $Ni(OH)_2$ and $Co_{0.03}Ni_{0.97}$LDH after 10 cycles.

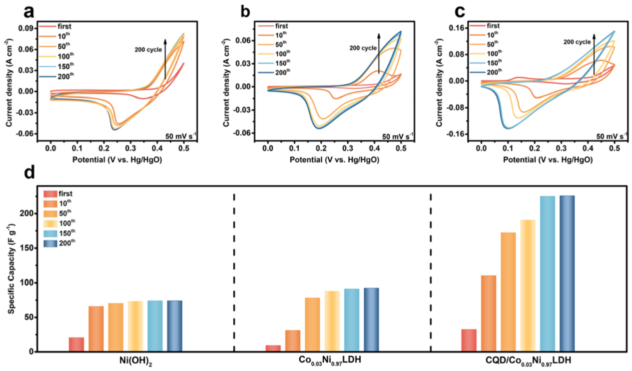

Fig. 1 CV curves of 200 cycles of activation at 50 mV s^{-1} for different electrode materials: (a) $Ni(OH)_2$, (b) $Co_{0.03}Ni_{0.97}$LDH, (c) CQD/$Co_{0.03}Ni_{0.97}$LDH. (d) Mass capacity at different activation cycle calculated from the CV curves.

After 200 CV cycles, CQD/$Co_{0.03}Ni_{0.97}$LDH possessed the best specific capacity, implying its irreversible change distinct from $Ni(OH)_2$ and $Co_{0.03}Ni_{0.97}$LDH. It indicates that the activated CQD/$Co_{0.03}Ni_{0.97}$LDH (A-CQD/$Co_{0.03}Ni_{0.97}$LDH) could deliver exceptionally high electrochemical activity. To observe the effect of the electrochemical activation process on the electrochemical properties of the individual electrode materials, the specific capacity calculated from the CV is shown in Fig. 1d. After 200 CV cycles, the obtained A-$Co_{0.03}Ni_{0.97}$LDH delivered a slightly improved specific capacity than that of A-$Ni(OH)_2$, suggesting that only low dose doping (3%) of Co is insufficient to increase the electrochemical performance of $Ni(OH)_2$. Furthermore, A-CQD/$Co_{0.03}Ni_{0.97}$LDH exhibited a high specific capacity being approximately 2.5 times that of A-$Co_{0.03}Ni_{0.97}$LDH, indicating that the introduction of CQD significantly improves the efficiency of electrochemical activation for the $Co_{0.03}Ni_{0.97}$LDH.

In addition, an irreversible oxidation peak at about 0.12 V can be observed in the first CV cycle for CQD/$Co_{0.03}Ni_{0.97}$LDH. To determine the origin of this peak, the 1^{st}–200^{th} CV curves of Co/CQD and CQD/$Ni(OH)_2$ (Fig. S1†) were obtained. The results show that the irreversible oxide peak has originated from Co^{2+} to Co^{3+}. However, the oxide peak in $Co_{0.03}Ni_{0.97}$LDH (Fig. 1b) is not observed. Therefore, the 1^{st}–200^{th} CV curves of CoNiLDH with different Ni to Co ratios were acquired and are shown in Fig. S2.† Obviously, the irreversible oxide peak appears only in the 1^{st} CV curve of the bimetallic CoNiLDH. However, the oxide peak of Co^{2+}/Co^{3+} is reversible in bare Co$(OH)_2$ (Fig. S2f†). Fig. S3a and b† display a part of the 1^{st} CV curve and the correlations between the peak current and the Ni to Co ratio. The peak current increased with the increase of the Co amount until the Co/Ni ratio is equal to 1 (Fig. S3b, c and Table S1†), which is consistent with the previous report that the optimal electrochemical performance is achieved at the Co/Ni ratio of 1 (Fig. S4†).[35] Then, the current decreased with the continual increase of the Co amount, which is attributed to the decrease from Co^{2+} to Co^{3+} caused by the reduced Ni content. The high positive correlation of $R^2 = 0.947$ in Fig. S3c† indicates that the peak current at about 0.12 V would be used to estimate the conversion from Co^{2+} to Co^{3+} in Co/Ni bimetallic LDH when the Co/Ni ratio is less than 1. The 1^{st} CV curves of $Co_{0.03}Ni_{0.97}$LDH and CQD/$Co_{0.03}Ni_{0.97}$LDH indicate that the introduction of CQDs can efficiently improve the transformation from Co^{2+} to Co^{3+}, resulting in the high concentration of Co^{3+} in A-CQD/$Co_{0.03}Ni_{0.97}$LDH.

Generally, different crystalline phases of electrode materials have different electrochemical activity.[36] The XRD patterns of electrode materials before and after electrochemical activation were obtained to reveal the possible crystalline phase transformation process that might have occurred during the CV cycle. As shown in Fig. 2a, both $Ni(OH)_2$ and A-$Ni(OH)_2$ show (003), (006), (101), (015) and (110) characteristic crystal planes of α-$Ni(OH)_2$, corresponding to a shift in the standard card (JCPDS No. 38-0715), which is mainly due to the interlayer CO_3^{2-}.[37,38] After the electrochemical activation, only crystalli-

This journal is © the Partner Organisations 2024

Published on 13 December 2023. Downloaded by Fail Open on 07/05/2025 8:52:43 AM.

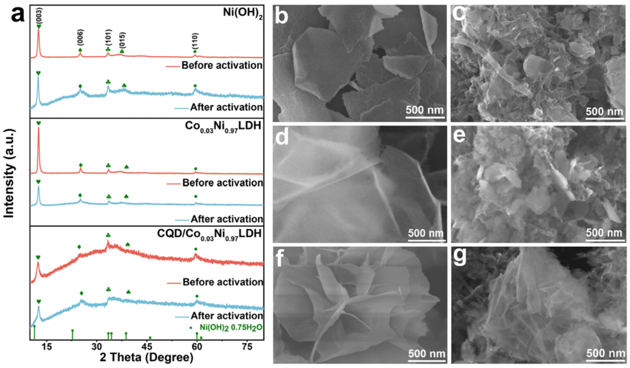

Fig. 2 (a) XRD patterns before and after CV activation. (b) and (c) SEM images of $Ni(OH)_2$ and A-$Ni(OH)_2$. (d) and (e) SEM images of $Co_{0.03}Ni_{0.97}$LDH and A-$Co_{0.03}Ni_{0.97}$LDH. (f) and (g) SEM images of CQD/$Co_{0.03}Ni_{0.97}$LDH and A-CQD/$Co_{0.03}Ni_{0.97}$LDH.

nity reduced, and no phase change occurred in A-$Ni(OH)_2$. Similarly, the XRD pattern of $Co_{0.03}Ni_{0.97}$LDH does not display the characteristic peaks of $Co(OH)_2$ and the electrochemical activation could influence the crystallinity rather than phase transformation. The XRD pattern of CQD/$Co_{0.03}Ni_{0.97}$LDH still shows a broad peak between 25 and 45°, which can be attributed to the CQDs (Fig. S5a†), and the characteristic peaks of α-$Ni(OH)_2$. A-CQD/$Co_{0.03}Ni_{0.97}$LDH also only exhibited reduced crystallinity. The above results confirm that the improved electrochemical capacity after the electrochemical activation process is not attributed to the phase transformation. SEM was used to observe the morphology and structural changes of the electrode materials after electrochemical activation. Fig. 2b shows a sheet-like structure of $Ni(OH)_2$ with little cross-linking between the individual nanosheets. After the CV activation (Fig. 2c), these large $Ni(OH)_2$ nanosheets were converted to fine A-$Ni(OH)_2$ nanosheets closely stacked together. Fig. 2d displays the $Co_{0.03}Ni_{0.97}$LDH nanosheets, which are thinner than the $Ni(OH)_2$ nanosheets and exhibit obvious curls at the edges. After the electrochemical activation, small A-$Co_{0.03}Ni_{0.97}$LDH nanosheets were formed and clustered together like A-$Ni(OH)_2$ (Fig. 2e). Fig. 2f indicates that the CQD/$Co_{0.03}Ni_{0.97}$LDH nanosheets were self-assembled to a flower-like structure possibly because of the inducing effect of the CQDs. After 200 cycles of CV activation, the flower-like structure was destroyed and these nanosheets were broken up to create tiny nanosheets, as shown in Fig. 2g. What is more, the specific surface area of the three electrodes does not change significantly after electrochemical activation (Fig. S6 and Table S2†). Fig. S7† displays the typical TEM images of Co/CQD. To observe the presence of CQDs, the TEM images of CQD/$Co_{0.03}Ni_{0.97}$LDH and A-CQD/$Co_{0.03}Ni_{0.97}$LDH are shown in Fig. S8 and S9.† Fig. S8a† exhibits the flower-like structure assembled by CQD/$Co_{0.03}Ni_{0.97}$LDH nanosheets. The HRTEM images (Fig. S8b–d†) show the obvious lattice fringe of 0.24 and 0.21 nm, corresponding to the (111) plane of $Co_{0.03}Ni_{0.97}$LDH and the (100) plane of CQDs.[39] The EDS mapping presented in Fig. S8e† indicates that the CQDs are uniformly dispersed on the surface of the $Co_{0.03}Ni_{0.97}$LDH nanosheets. After the electrochemical activation, the flower-like structure was destroyed and these large nanosheets were transformed into tiny nanosheets (Fig. S9a†). CQDs can still be observed on the surface of the tiny nanosheets (Fig. S9b–d†). The EDS mapping in Fig. S9e† further confirms the uniform existence of CQDs. The above SEM and TEM observation indicate that all three hydroxides tend to shift towards thinner nanosheets, which will give a larger specific surface area and provide more active sites for electrochemical reaction, resulting in the improvement of energy storage density.

XPS was performed to analyse the chemical elemental composition and valence information before and after the electrochemical activation. Fig. 3a shows the Co $2p_{3/2}$ high resolution XPS spectra of $Co_{0.03}Ni_{0.97}$LDH and CQD/$Co_{0.03}Ni_{0.97}$LDH, where 784.6 eV belongs to the satellite peak of Co (Sat.) and the broad main peak at 779.2 eV can be attributed to the $2p_{3/2}$ signal of the element Co. The $2p_{3/2}$ signal can fitted into two peaks at 778.9 eV and 780.8 eV corresponding to Co^{3+} and Co^{2+} species, respectively.[40] Before activation, both Co^{3+} and Co^{2+} species could be observed, and the content of Co^{3+} in $Co_{0.03}Ni_{0.97}$LDH was up to 57.5% (Fig. 3b) but only 28.9% in CQD/$Co_{0.03}Ni_{0.97}$LDH, which is mainly attributed to the reducibility of CQDs inhibiting the oxidation of Co^{2+} during the hydrothermal reaction (Fig. S10a†). After CV activation, the content of Co^{3+} increased in A-$Co_{0.03}Ni_{0.97}$LDH and A-CQD/$Co_{0.03}Ni_{0.97}$LDH owing to the irreversible oxidation of Co^{2+}.[23] Unexpectedly, the Co^{3+} content in A-CQD/$Co_{0.03}Ni_{0.97}$LDH was 70.7%, which is higher than that of A-$Co_{0.03}Ni_{0.97}$LDH (62.1%). This may be due to the strong interaction between CQD and Co,[41] which accelerates the charge transport on the Co atom in the electrochemical process, resulting in more Co^{2+} being oxidized to Co^{3+}. During the process of energy storage, Co^{3+} can be transformed into Co^{4+} with higher energy density resulting in enhanced energy storage performance of the electrode material.[42] Therefore, the produced high concentration of Co^{3+} will be conducive to improving the electrochemical performance of A-CQD/$Co_{0.03}Ni_{0.97}$LDH.

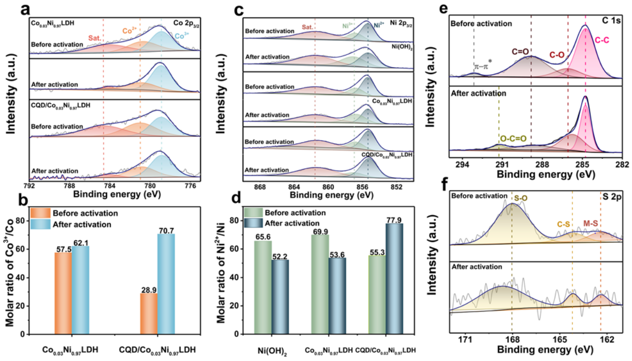

Fig. 3 XPS spectra of (a) Co $2p_{3/2}$ and (c) Ni $2p_{3/2}$ of $Ni(OH)_2$, $Co_{0.03}Ni_{0.97}$LDH and CQD/$Co_{0.03}Ni_{0.97}$LDH before and after electrochemical activation. (b) Co^{3+} content and (d) Ni^{2+} content calculated from XPS spectra. (e) C 1s and (f) S 2p XPS spectra of CQD/$Co_{0.03}Ni_{0.97}$LDH before and after electrochemical activation.

Published on 13 December 2023. Downloaded by Fail Open on 07/05/2025 8:52:43 AM.

Fig. 3c displays the XPS spectra of Ni $2p_{3/2}$. The broad peak at 855.5 eV can deconvoluted into two species of Ni^{2+} at 855.3 eV and Ni^{3+} at 856.8 eV.[43] Before activation, the Ni^{2+} content in $Ni(OH)_2$ (65.6%) and $Co_{0.03}Ni_{0.97}$LDH (69.9%) was closer (Fig. 3d). However, 55.3% of Ni^{2+} for CQD/$Co_{0.03}Ni_{0.97}$LDH was lower than the previous two samples due to the oxidation of Co^{3+} (Fig. S10a†). After electrochemical activation, the fitted peaks corresponding to the Ni^{2+} and Ni^{3+} species were still located at 855.3 and 856.8 eV, indicating that no change had occurred in the chemical environment of Ni^{2+} and Ni^{3+}. However, the original equilibrium of Ni^{2+}/Ni^{3+} was destroyed and the Ni^{2+} content in both $Ni(OH)_2$ and $Co_{0.03}Ni_{0.97}$LDH decreased after CV activation (Fig. 3d). In $Ni(OH)_2$, 13.4% of Ni^{2+} was converted to Ni^{3+} because of the irreversible oxidation during the CV cycle. Owing to the synergistic effect of irreversible oxidation reaction during CV and the oxidation of Co^{3+} available (Fig. 3a), 16.3% of Ni^{2+} was oxidized to Ni^{3+} in A-$Co_{0.03}Ni_{0.97}$LDH. Unlike $Ni(OH)_2$ and $Co_{0.03}Ni_{0.97}$LDH, the concentrations of both Co^{3+} and Ni^{2+} species increased in A-CQD/$Co_{0.03}Ni_{0.97}$LDH, and 77.9% of Ni^{2+} is much more than that in A-$Ni(OH)_2$ and A-$Co_{0.03}Ni_{0.97}$LDH. This unique phenomenon may be attributed to the reducibility and high conductivity of the CQDs.[44] During the CV activation process, Co^{2+} is oxidized to Co^{3+}, one electron lost in Co^{2+} is preferentially transmitted through the CQD with high conductivity due to the close connection between Co^{2+} and the CQD.[44] Ultimately, the electrons in the CQDs are retransmitted to the surrounding Ni^{3+} to generate Ni^{2+}, forming a mechanism of electron transfer based on CQDs. Furthermore, the possible bonding between Co^{3+} and CQD would reduce the oxidation ability of Co^{3+}, allowing high concentrations of Co^{3+} and Ni^{2+} to co-exist in A-CQD/$Co_{0.03}Ni_{0.97}$LDH.

To further investigate the role of CQDs in the electrochemical activation, the XPS spectra of C 1s for CQD/$Co_{0.03}Ni_{0.97}$LDH are shown in Fig. 3e. Three characteristic peaks for C–C (284.8 eV), C–O (285.7 eV) and C═O (288.8 eV) are assigned to the CQDs (Fig. S10b†).[45] The appearance of the π–π* peak may be attributed to the rearrangement of the sp^2 carbon network in CQDs during the hydrothermal reaction. After CV activation, the π–π* peak disappeared mainly because of the bonding between C and Co. In addition, the obviously decreased peak of C═O and the increased intensity of the C–O peak as well as the appearance of the O–C═O peak indicate that part of the C═O in CQD was oxidized to C–O and O–C═O during the activation process, further confirming that CQD participates in the activation process of $Co_{0.03}Ni_{0.97}$LDH. Fig. 3f presents the XPS spectra of S 2p, which fit to S–O (168.6 eV), C–S (164.1 eV) and metal–S (M–S, 162.4 eV). Compared with the S 2p signal of pristine Co ion-modified CQDs (Co/CQD) shown in Fig. S10c,† the intensity of the C–S and metal–S peaks decreased after the hydrothermal reaction, suggesting that the adsorbed Co ions on the CQDs were transferred into the structure of LDH. Moreover, as shown in Fig. S11,† most of the S species in the CQDs were oxidized into SO_4^{2-} during the hydrothermal reaction and the following CV activation.[22] However, the relative intensity of the C–S and M–S signals increased after CV activation.

XAFS measurements were carried out to reveal the coordination environment of Ni and Co in CQD/$Co_{0.03}Ni_{0.97}$LDH before and after electrochemical activation. The X-ray absorption near-edge structure spectra of the Ni K-edges in A-CQD/$Co_{0.03}Ni_{0.97}$LDH shifted to lower energy compared to that in CQD/$Co_{0.03}Ni_{0.97}$LDH (Fig. 4a), suggesting that more Ni^{3+} had been converted to Ni^{2+} after the electrochemical activation. It demonstrates that the introduction of CQDs can effectively promote the transformation from Ni^{3+} to highly active Ni^{2+} during electrochemical activation. With the increase of Ni^{2+} amount in the A-CQD/$Co_{0.03}Ni_{0.97}$LDH, the electron spin density in the $d_{x^2-y^2}$ orbital of Ni^{2+} can be distributed over the Ni–O slabs and hence relieve the Jahn–Teller distortion caused by Ni^{3+} and Co^{2+}.[46,47] As evident in the inset of Fig. 4b, the shifting of the Co K-edge position towards higher energy after CV activation indicates an increase of Co^{3+} in Co element, which is consistent with the XPS results. The k^3x oscillation curves of the Ni K-edges in CQD/$Co_{0.03}Ni_{0.97}$LDH and A-CQD/$Co_{0.03}Ni_{0.97}$LDH (Fig. 4c) exhibit only a slight decrease in the oscillation amplitude, denoting that the change in the coordination environment of the Ni atoms is weak during the electrochemical activation process. In contrast, the Co K-edge k^3x oscillation curve (Fig. 4d) varies considerably after CV activation, illustrating that the coordination environment of Co atoms undergoes significant changes after CV activation. Fig. 4e and f demonstrate the wavelet transition (WT) of the Ni

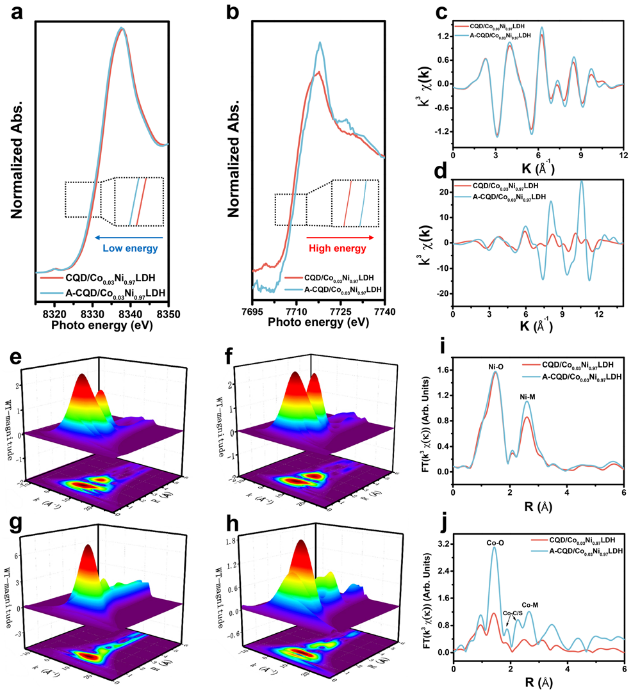

Fig. 4 XANES spectra of (a) Ni K-edge and (b) Co K-edge for CQD/$Co_{0.03}Ni_{0.97}$LDH before and after electrochemical activation. (c) Ni K-edge EXAFS oscillation functions $k^3\chi(k)$ and (d) Co K-edge EXAFS oscillation functions $k^3\chi(k)$. Wavelet transform EXAFS spectra of (e and f) Ni K-edge and (g and h) Co K-edge. Fourier transform (FT) k^3-weighted $\chi(k)$ function of the EXAFS spectra for (i) Ni K-edge and (j) Co K-edge.

This journal is © the Partner Organisations 2024

Published on 13 December 2023. Downloaded by Fail Open on 07/05/2025 8:52:43 AM.

K-edge, where the two WT maximum signals near 1.48 and 2.59 Å can be associated with Ni–O and Ni–metal (Ni–M) bonds, respectively.[48] The scattering path signal intensity at 1.48 Å for A-CQD/$Co_{0.03}Ni_{0.97}$LDH is not different from that of CQD/$Co_{0.03}Ni_{0.97}$LDH, whereas the intensity of the signal at 2.59 Å increases, suggesting that the Ni–M bond in A-CQD/$Co_{0.03}Ni_{0.97}$LDH had improved. The obvious signal at 1.43 Å in the Co K-edge EXAFS WT analysis (Fig. 4g) is attributed to the Co–O bonding in CQD/$Co_{0.03}Ni_{0.97}$LDH. After CV activation (Fig. 4h), the Co–O bond strength of A-CQD/$Co_{0.03}Ni_{0.97}$LDH increases significantly after electrochemical activation. Moreover, the signals of Co–C/S and Co–metal (Co–M) appear at 1.87, 2.25 and 2.64 Å,[49] demonstrating the presence of strong bonding between Co and the functional groups on the CQDs after CV activation. The Fourier transform $k^3\chi(k)$ oscillation function can be used to study in-depth the changes in the coordination environment of Ni and Co before and after activation. Fig. 4i shows the Ni–R spatial curves. Fig. S12 and Table S3† give the fitting results and detailed information about the Ni coordination. There is only one characteristic peak at 1.48 Å in the first path, which is the scattering path of the Ni–O bond. The coordination number of Ni–O before and after activation has no obvious change and close to 6. Similarly, the coordination number of Ni–M at the 2.59 Å path is slightly elevated from 5.8 to 6.1 mainly since some of the Co enter the $Ni(OH)_2$ lattice after electrochemical activation. The Co–R space curve (Fig. 4j) exhibits a prominent Co–O peak at 1.43 Å and a weak Co–C/S peak at 1.87 Å in CQD/$Co_{0.03}Ni_{0.97}$LDH. It suggests that the Co atoms are mainly bonded to O atoms in CQD/$Co_{0.03}Ni_{0.97}$LDH. The fitting coordination number of Co–O is approximately 5 (Fig. S13 and Table S4†). The weak intensity of Co–C/S indicates that the interaction between Co and CQD is unstable before the electrochemical activation. After the electrochemical activation, the intensity of Co–O in A-CQD/$Co_{0.03}Ni_{0.97}$LDH shows a clear increase, implying the improved bonding between Co with O. Moreover, the intensity of the Co–M peak increases, which can be attributed to the increase in the number of edge-sharing CoO_6 octahedra formed after partial Co substitution for Ni.[50] Furthermore, the increased intensity of Co–C/S peaks suggests tighter bonding between Co and CQD instead of separating from CQD after the electrochemical activation, which is conducive to the transport of electrons from Co to CQD, resulting in the generation of greater numbers of stable Co^{3+}. In addition, the fitting calculations indicate a 5-coordination structure of Co in A-CQD/$Co_{0.03}Ni_{0.97}$LDH consisting of 3-coordination of Co–O and 2-coordination of Co–C/S. This 5-coordination structure of Co has the best redox energy barrier, which is conducive to reversible charge storage and high redox activity,[15] leading to the improved electrochemical performance of A-CQD/$Co_{0.03}Ni_{0.97}$LDH.

To further elucidate the intrinsic mechanism of CQD for enhancing energy storage of $Co_{0.03}Ni_{0.97}$LDH, density functional theory (DFT) calculations were performed (Text S2†), as shown in Fig. 5. Fig. 5a–c show the optimized structures of A-$Ni(OH)_2$, A-$Co_{0.03}Ni_{0.97}$LDH, and A-CQD/$Co_{0.03}Ni_{0.97}$LDH, respectively. The coexistence of Co^{3+} and Ni^{2+} in A-CQD/$Co_{0.03}Ni_{0.97}$LDH is further revealed by the 3D differential charge density shown in Fig. 5d and Fig. S14.† The Hirshfeld charge of Ni^{2+} in A-$Ni(OH)_2$ is 0.14*e*. The charge of Ni^{2+} is increased to 0.17*e* in A-$Co_{0.03}Ni_{0.97}$LDH, indicating that a little Co^{3+} doping can improve the oxidation of Ni^{2+} to form Ni^{3+}. However, the charge of Ni^{2+} in A-CQD/$Co_{0.03}Ni_{0.97}$LDH only increases slightly to 0.15*e* in the presence of Co^{3+}. In addition, the Hirshfeld charge of Co^{3+} in A-CQD/$Co_{0.03}Ni_{0.97}$LDH is 0.09*e*, which is much lower than that in A-$Co_{0.03}Ni_{0.97}$LDH (0.17*e*).

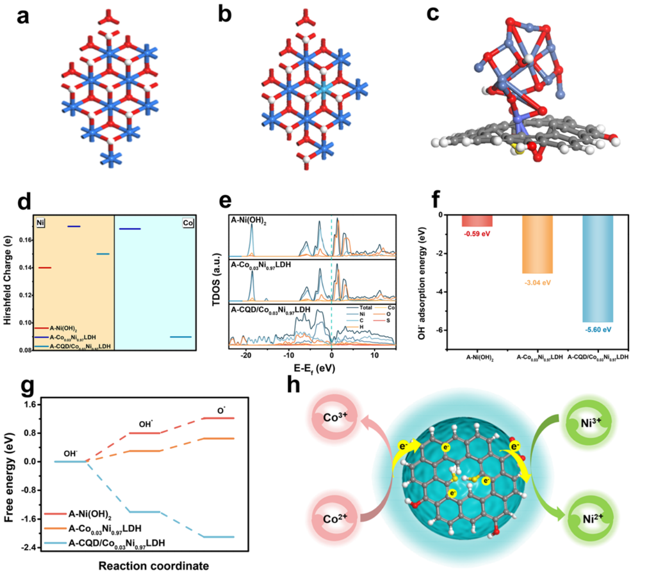

Fig. 5 (a–c) Structural model diagrams for A-$Ni(OH)_2$, $Co_{0.03}Ni_{0.97}$LDH and A-CQD/$Co_{0.03}Ni_{0.97}$LDH. (d) Hirshfeld charge for Co and Ni, (e) corresponding total density of states diagram. (f) Adsorption energy for OH^-, (g) free energy diagram of charging storage. (h) Mechanism diagram.

The above results indicate that the bonding between CQDs and Co can efficiently optimize the charge distribution of Co^{3+} formed after the electrochemical activation, so that it can exist more stably. Furthermore, the stable Co^{3+} in A-CQD/$Co_{0.03}Ni_{0.97}$LDH does not cause a significant increase in the charge of the surrounding Ni^{2+}; therefore, the high concentration of Ni^{2+} can be maintained in A-CQD/$Co_{0.03}Ni_{0.97}$LDH. The total density of states (TDOS) and the contribution of each element are shown in Fig. 5e. Compared to A-$Ni(OH)_2$ and A-$Co_{0.03}Ni_{0.97}$LDH, A-CQD/$Co_{0.03}Ni_{0.97}$LDH displays a higher TDOS at the Fermi energy level, which is mainly contributed by CQDs and Ni, indicating that the introduction of CQDs can enhance the metallicity of the material as well as improve the conductivity to promote electron transfer,[51] which facilitates the mitigation of the Jahn–Teller distortion.[52] To evaluate the difficulty of the electrochemical reaction, the adsorption energy of OH^- and the free energy for protonation reactions are shown in Fig. 5f and g. The lowest adsorption energy of OH^- (−5.6 eV) for A-CQD/$Co_{0.03}Ni_{0.97}$LDH indicates that A-CQD/$Co_{0.03}Ni_{0.97}$LDH adsorbs OH^- more readily than A-Ni

Published on 13 December 2023. Downloaded by Fail Open on 07/05/2025 8:52:43 AM.

$(OH)_2$ and A-$Co_{0.03}Ni_{0.97}$LDH to carry out the reactions as shown in the following processes.[53]

$$* + OH^- \rightleftharpoons OH* + e^- \tag{5}$$

$$OH* + OH^- \rightleftharpoons O* + H_2O + e^- \tag{6}$$

The free energy of both reactions is positive on A-$Ni(OH)_2$ and A-$Co_{0.03}Ni_{0.97}$LDH. Moreover, the energy required for A-$Co_{0.03}Ni_{0.97}$LDH is lower than that for A-$Ni(OH)_2$, confirming that the doping of Co can effectively improve the ability of protonation during the energy storage process. The modification of CQDs to form A-CQD/$Co_{0.03}Ni_{0.97}$LDH can decrease the free energy further from positive to negative values of −1.4 and −2.1 eV, respectively. It indicates that A-CQD/$Co_{0.03}Ni_{0.97}$LDH exhibits the lowest redox reaction energy barrier among all samples, resulting in the best redox activity and the highest electrochemical capacity. According to the above characterization and theoretical calculations, we propose the CQD-based electrochemical activation mechanism shown in Fig. 5h. During the activation process, the electrons generated during the oxidation of Co^{2+} to Co^{3+} are transported to Ni^{3+} through highly conductive CQDs, causing the reduction of Ni^{3+} to Ni^{2+} again. In addition, the strong interaction between CQD and Co can optimize the charge distribution of Co^{3+}, resulting in the coexistence of high concentrations of Co^{3+} and Ni^{2+}. CQDs act as an electron transport bridge and valence stabilizer during the whole process. Even though CQDs themselves have poor energy storage activity, their electrochemical activation can modulate the generation of more Co^{3+} and Ni^{2+}, which are the active sites for energy storage. Moreover, the redox barrier of the reaction system is decreased. These are the reasons for CQDs enhancing the synergistic effect between Ni and Co in bimetallic LDH.

Electrochemical properties in the asymmetric supercapacitor

Electrochemical properties of A-$Ni(OH)_2$, A-$Co_{0.03}Ni_{0.97}$LDH and A-CQD/$Co_{0.03}Ni_{0.97}$LDH were evaluated in 6 M KOH using a 3-electrode system. Fig. 6a displays the CV plots at the scan rate of 3 mV s^{-1}. The obvious redox peaks indicate that the three materials are battery-type electrode materials. In addition, two oxidation peaks can be observed in A-$Co_{0.03}Ni_{0.97}$LDH and A-CQD/$Co_{0.03}Ni_{0.97}$LDH. The oxidation reaction at higher potential can be attributed to the oxidation of Co^{3+} to Co^{4+}, and the peak current in A-CQD/$Co_{0.03}Ni_{0.97}$LDH is significantly higher than in A-$Co_{0.03}Ni_{0.97}$LDH, indicating more conversion from Co^{3+} to Co^{4+}, which is beneficial for the improved capacity performance of A-CQD/$Co_{0.03}Ni_{0.97}$LDH. The Faraday reactions are shown in the eqn (7)–(9).

$$Ni(OH)_2 + OH^- \rightleftharpoons NiOOH + H_2O + e^- \tag{7}$$

$$Co(OH)_2 + OH^- \rightleftharpoons CoOOH + H_2O + e^- \tag{8}$$

$$CoOOH + OH^- \rightleftharpoons CoO_2 + H_2O + e^- \tag{9}$$

As shown in Fig. S15,† the bigger area of A-CQD/$Co_{0.03}Ni_{0.97}$LDH suggests that its specific capacity is higher than that of A-$Ni(OH)_2$ and A-$Co_{0.03}Ni_{0.97}$LDH. Fig. 6b shows the GCD curves at 1 A g^{-1}. The clear redox plateau further confirms their battery-type characteristic. These GCD curves hold the symmetry during charge and discharge, denoting their good reversibility and superior Coulombic efficiency. According to the discharge curves, the specific capacities of A-$Ni(OH)_2$ and A-$Co_{0.03}Ni_{0.97}$LDH are almost the same, illustrating that the low amount of Co doping is insufficient for improving the capacity of $Ni(OH)_2$. Compared with A-$Ni(OH)_2$ and A-$Co_{0.03}Ni_{0.97}$LDH, A-CQD/$Co_{0.03}Ni_{0.97}$LDH displays significantly longer discharge time, further confirming its higher capacity. At a current density of 1 A g^{-1}, the specific capacity of A-CQD/$Co_{0.03}Ni_{0.97}$LDH is 2408 F g^{-1}, much more than that of A-$Co_{0.03}Ni_{0.97}$LDH (1026 F g^{-1}) and A-$Ni(OH)_2$ (1094 F g^{-1}). To clarify the contribution of the high capacity, Fig. S16† illustrates the capacity performance of A-Co/CQD, in which the low specific capacity of 75 F g^{-1} at 1 A g^{-1} indicates that the high capacity of A-CQD/$Co_{0.03}Ni_{0.97}$LDH has mainly originated from the highly active $Co_{0.03}Ni_{0.97}$LDH. Similarly, the electrochemical performance of A-CQD/$Ni(OH)_2$ had only slightly improved, suggesting that the effect of CQDs on $Ni(OH)_2$ is more limited and much less than that of Co/CQD (Fig. S17†). Furthermore, A-CQD/$Co_{0.03}Ni_{0.97}$LDH continued to possess a high specific capacity of 1665 F g^{-1} at 10 A g^{-1} in comparison with 830 and 880 F g^{-1} for A-$Ni(OH)_2$ and A-$Co_{0.03}Ni_{0.97}$LDH at 10 A g^{-1} (Fig. 6c and Fig. S18†). Electrochemical impedance spectroscopy (EIS) was performed to analyse the role of Co doping and CQD modification on the electron/charge transfer

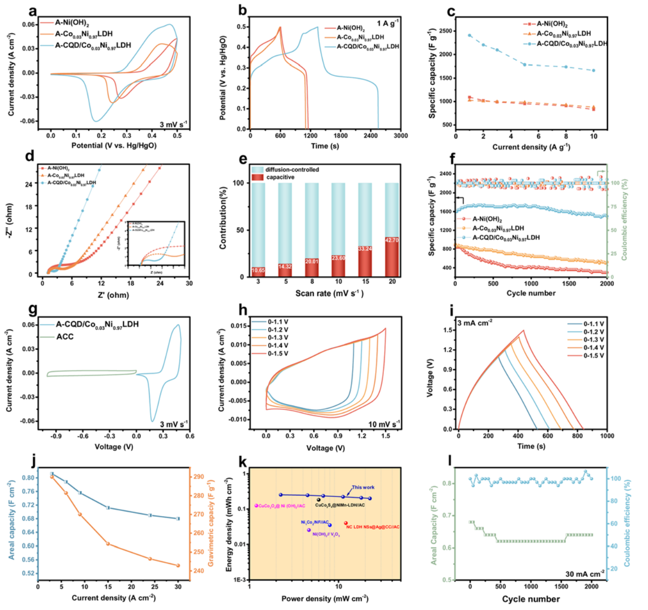

Fig. 6 (a) CV curves at 3 mV s^{-1}. (b) GCD curves at 1 A g^{-1}. (c) Mass specific capacity and (d) Nyquist plots of A-$Ni(OH)_2$, A-$Co_{0.03}Ni_{0.97}$LDH and A-CQD/$Co_{0.03}Ni_{0.97}$LDH electrodes. (e) Capacitance contribution of A-CQD/$Co_{0.03}Ni_{0.97}$LDH. (f) Cycling stability of A-$Ni(OH)_2$, A-$Co_{0.03}Ni_{0.97}$LDH and A-CQD/$Co_{0.03}Ni_{0.97}$LDH electrodes at 10 A g^{-1}. (g) CV curves of ACC and A-CQD/$Co_{0.03}Ni_{0.97}$LDH electrodes at 3 mV s^{-1}. (h) CV and (i) GCD curves of A-CQD/$Co_{0.03}Ni_{0.97}$LDH//ACC ASC under different voltage windows. (j) Specific capacity of the ASC at different current densities. (k) Ragone plot of the ASC compared to previous reported. (l) Cycling stability of the ASC at 30 mA cm^{-2}.

This journal is © the Partner Organisations 2024

Published on 13 December 2023. Downloaded by Fail Open on 07/05/2025 8:52:43 AM.

of A-CQD/$Co_{0.03}Ni_{0.97}$LDH. Fig. 6d and Fig. S19† present the obtained Nyquist plots, including an arc in the medium and high frequencies and a straight line in the low-frequency. Based on the equivalent circuit (Fig. S20†), the calculated internal resistance (R_s) and charge transfer resistance (R_{ct}) are listed in Table S5.† The large R_{ct} (2.3 Ω) of A-$Ni(OH)_2$ is reduced to 2.0 Ω of A-$Co_{0.03}Ni_{0.97}$LDH because of Co doping, and further obviously decreases by the increase of Co. It indicates that Co doping is mainly responsible for the improvement of charge transfer capability to accelerate the reaction kinetics of electrode materials. For A-CQD/$Co_{0.03}Ni_{0.97}$LDH, R_s and R_{ct} reduce to 1.1 and 0.9 Ω, respectively, which shows that the modification of CQD can effectively improve the conductivity of $Co_{0.03}Ni_{0.97}$LDH. To further understand the electrochemical kinetics of A-CQD/$Co_{0.03}Ni_{0.97}$LDH, the diffusion-controlled contribution and the capacitive contribution are analysed according to the equations in Text S1.†[54] As shown in Fig. S21,† the *b*-value is obtained by fitting the slope of the linear line of lg(ν) to lg(i) in the CV curve. When the *b* value is 1, it indicates a capacitive behaviour; as *b* value is 0.5, it means a diffusion-controlled behaviour. The *b* values of 0.375 and 0.339 for A-CQD/$Co_{0.03}Ni_{0.97}$LDH indicate that the battery-type redox kinetics dominate the charge storage process in A-CQD/$Co_{0.03}Ni_{0.97}$LDH and the kinetic behaviour mainly is controlled by diffusion. In addition, the methods as proposed by Pu *et al.*[55] were used to quantify the contribution of capacitive or diffusive-controlled contributions. The approaches of eliminating residual currents and reducing polarization can better distinguish the capacitive and diffusive contributions, improving the reliability of quantifying results.[56] The capacitive contribution of A-CQD/$Co_{0.03}Ni_{0.97}$LDH is shown in Fig. S22.† At the scan rate of 3 mV s^{-1}, the diffusion-controlled contribution is 89.4% for the capacity of A-CQD/$Co_{0.03}Ni_{0.97}$LDH (Fig. 6e), and the proportion of the diffusion-controlled contribution decreases with the increase of scan rate. As the scan rate increases to 20 mV s^{-1}, the diffusion-controlled contribution decreases to 57.3%. The previous work reported that the diffusion-controlled behaviour at high scan rates failed to achieve rapid ion transfer for fast electrochemical reactions.[57] However, A-CQD/$Co_{0.03}Ni_{0.97}$LDH can maintain a high diffusion-controlled contribution at high scan rates, indicating that the synergistic effect of CQD modification and the low Co doping can effectively improve the rapid charge/ion transfer at the electrode to achieve fast reaction kinetics and complete an efficient redox reaction. The cycling stability of each electrode was further investigated using a continuous GCD test at 10 A g^{-1} as shown in Fig. 6f. After 2000 cycles, the specific capacity of A-$Ni(OH)_2$ decreases seriously to 300 F g^{-1}, A-$Co_{0.03}Ni_{0.97}$LDH can remain 520 F g^{-1}, indicating that the low Co doping can improve the stability of the electrode, but still unsatisfactory. The A-CQD/$Co_{0.03}Ni_{0.97}$LDH electrode shows an excellent cycling stability with a high specific capacitance of 1500 F g^{-1} after 2000 cycles, which indicates that the combination of CQD introduction and low Co doping can efficiently improve the electrochemical performance of $Ni(OH)_2$.

For verifying the practical application prospects of the electrode materials, the asymmetric supercapacitors (ASC) were assembled using A-CQD/$Co_{0.03}Ni_{0.97}$LDH electrodes as the positive electrode, activated carbon cloth (ACC) as the negative electrode, 6 M KOH as the electrolyte and glass fiber filter paper (GF) as the separator, denoted as A-CQD/$Co_{0.03}Ni_{0.97}$LDH//ACC (Fig. S23†). The electrochemical properties of ACC are shown in Fig. S24.† ACC exhibits a large double layer capacitance between the voltage window of −1 V and 0 V. The areal capacity of ACC reaches 1.8 F cm^{-2} at 3 mA cm^{-2} and remains 1.3 F cm^{-2} at 30 mA cm^{-2}, showing superior capacitance retention. Fig. 6g shows the CV curves of the A-CQD/$Co_{0.03}Ni_{0.97}$LDH@CC and ACC electrodes. No significant polarization indicates that the device has a stable operating voltage window from 0 to 1.5 V (Fig. 6h and i). The nearly rectangular shape containing a clear redox peak suggests the presence of both double layer and battery-type capacity at 0 to 1.5 V. With the increase of scan rate, no deformation occurred for the CV curves suggests that the device has an ideal rate capability (Fig. S25a†). According to the GCD curves of A-CQD/$Co_{0.03}Ni_{0.97}$LDH//ACC ASC presented in Fig. S25b† and Fig. 6j, the calculated areal capacity is 0.82 F cm^{-2} (290 F g^{-1}) at 3 mA cm^{-2} and still maintains 0.68 F cm^{-2} (243 F g^{-1}) at 30 mA cm^{-2}. The Ragone plot (Fig. 6k) shows that the assembled device possesses a high energy density of 0.25 mW h cm^{-2} at a power density of 2.25 mW cm^{-2} and still maintains an energy density of 0.2 mW h cm^{-2} even at power densities up to 22.5 mW cm^{-2}. Compared to the recently reported CoNiLDH-based asymmetric devices (Table S6†), the A-CQD/$Co_{0.03}Ni_{0.97}$LDH//ACC ASC demonstrates superior performance. The cycling stability of the ASC was tested using galvanostatic GCD at 30 mA cm^{-2}. After 2000 cycles, the device still delivers an areal capacity of 0.64 F cm^{-2}, suggesting excellent cycling stability (Fig. 6l).

Electrochemical properties in a Ni–Zn battery

The electrochemical properties of A-CQD/$Co_{0.03}Ni_{0.97}$LDH were further evaluated in an aqueous Ni–Zn battery. Fig. 7a shows the schematic diagram of the assembled Ni–Zn battery, where A-CQD/$Co_{0.03}Ni_{0.97}$LDH and a commercial zinc flake is the anode and cathode, 6 M KOH + 0.5 M $Zn(CH_3COO)_2$ aqueous solution is the electrolyte and GF is the separator. A pair of obvious redox peaks in CV curves (Fig. 7b) for A-$Ni(OH)_2$//Zn and A-CQD/$Co_{0.03}Ni_{0.97}$LDH//Zn batteries at 0.1 mV s^{-1} can be attributed to the following electrochemical reactions.

Cathode:

$$\mathrm{Zn} + 4\mathrm{OH}^- \rightleftharpoons [\mathrm{Zn(OH)}_4]^{2-} + 2e^- \tag{10}$$

Anode:

$$\mathrm{Ni(OH)}_2 + [\mathrm{Zn(OH)}_4]^{2-} \rightleftharpoons \mathrm{NiOOH} + \mathrm{Zn}^{2+} + 3\mathrm{OH}^- + e^- \tag{11}$$

Published on 13 December 2023. Downloaded by Fail Open on 07/05/2025 8:52:43 AM.

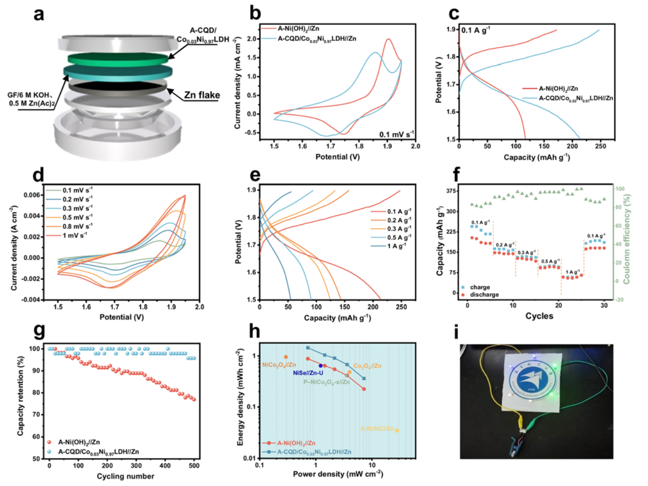

Fig. 7 (a) Structure of the A-CQD/$Co_{0.03}Ni_{0.97}$LDH//Zn battery. (b) CV curves (c) GCD curves of the A-$Ni(OH)_2$//Zn and A-CQD/$Co_{0.03}Ni_{0.97}$LDH//Zn battery. (d) CV curves at different scan rates. (e) GCD curves at different current densities and (f) rate performance of the A-CQD/$Co_{0.03}Ni_{0.97}$LDH//Zn battery. (g) Cycling stability. (h) Ragone plots of A-$Ni(OH)_2$//Zn and A-CQD/$Co_{0.03}Ni_{0.97}$LDH//Zn batteries. (i) Photograph of LED lamps powered by the A-CQD/$Co_{0.03}Ni_{0.97}$LDH//Zn battery.

$$Co(OH)_2 + [Zn(OH)_4]^{2-} \rightleftharpoons CoO_2 + Zn^{2+} + 2H_2O + 2OH^- + 2e^- \tag{12}$$

The redox peaks of both batteries show good symmetry, illustrating their good reversibility. The CV area of A-CQD/$Co_{0.03}Ni_{0.97}$LDH//Zn is obviously higher than that of A-Ni$(OH)_2$//Zn. Fig. 7c shows the GCD curves for A-Ni$(OH)_2$//Zn and A-CQD/$Co_{0.03}Ni_{0.97}$LDH//Zn at 0.1 A g^{-1}. Both batteries have a high discharge plateau (approximately 1.6 V–1.7 V). According to the discharge curve, the A-CQD/$Co_{0.03}Ni_{0.97}$LDH//Zn delivers a higher capacity of 213 mA h g^{-1} than 117 mA h g^{-1} of the A Ni$(OH)_2$//Zn at a current density of 0.1 A g^{-1}. As shown in Fig. 7d and e and Fig. S26,† with the increase of the scan rate from 0.1 to 1 mV s^{-1} and current density from 0.1 to 1 A g^{-1}, CV and GCD curves for the A-CQD/$Co_{0.03}Ni_{0.97}$LDH//Zn battery exhibit smaller deformation than those of the A-Ni$(OH)_2$//Zn, indicating its higher rate capability.

To evaluate the rate performance of the batteries in-depth, the two batteries were tested using the continued GCD method (Fig. 7e and Fig. S26b†). The reversible capacities of the A-CQD/$Co_{0.03}Ni_{0.97}$LDH//Zn battery (Fig. 7f) are 148, 127, 96, and 58 mA h g^{-1} at the current densities of 0.2, 0.3, 0.5 and 1 A g^{-1}, respectively, which are much higher than those of the A-Ni$(OH)_2$//Zn battery (Fig. S26c†). After 25 cycles, the A-CQD/$Co_{0.03}Ni_{0.97}$LDH//Zn battery still delivered a reversible capacity of 165 mA h g^{-1} at 0.1 A g^{-1}. Fig. 7g displays the cycling performance of the A-CQD/$Co_{0.03}Ni_{0.97}$LDH//Zn and A-Ni$(OH)_2$//Zn batteries. At a current density of 0.3 A g^{-1}, the A-CQD/$Co_{0.03}Ni_{0.97}$LDH battery exhibits 95.7% capacity retention after 500 cycles, which is better than 76.9% retention for A-Ni$(OH)_2$//Zn battery. Fig. 7h shows a comparison of the energy density-power density curves of the two batteries. The A-CQD/$Co_{0.03}Ni_{0.97}$LDH//Zn battery achieves an energy density of 1.44 mW h cm^{-2} at a power density of 0.72 mW cm^{-2} and retains an energy density of 0.36 W h cm^{-2} even when the power density reaches 7.2 W cm^{-2}, significantly better than that of the A-Ni$(OH)_2$//Zn battery and other Ni–Zn batteries (Table S7†). Furthermore, to evaluate the potential in practical applications, two A-CQD/$Co_{0.03}Ni_{0.97}$LDH//Zn batteries connected in series can successfully light up six different coloured LED lamps (Fig. 7i).

Conclusions

In summary, A-CQD/$Co_{0.03}Ni_{0.97}$LDH nanosheets were successfully fabricated using the CV cycle activation process. The high electrochemical activity of A-CQD/$Co_{0.03}Ni_{0.97}$LDH is mainly attributed to the optimized valence and coordination structure of Ni and Co in $Co_{0.03}Ni_{0.97}$LDH during the electrochemical activation. XPS spectra indicated that the high concentrations of Co^{3+} and Ni^{2+} can coexist in $Co_{0.03}Ni_{0.97}$LDH because of the excellent electron transfer of CQDs. EXAFS revealed the change from the originally 6-coordinated Co to 5-coordinated Co and strong valence bonding (Co–C/S) with CQDs after electrochemical activation. The DFT results further confirmed that CQDs play a crucial role in regulating the charge distribution of Ni and Co, which ensures that Co^{3+} and Ni^{2+} can be present in high concentrations simultaneously, thereby mitigating the adverse effects of the Jahn–Teller aberration. Furthermore, the excellent conductivity of CQDs not only can enhance the electron transport capability of A-CQD/$Co_{0.03}Ni_{0.97}$LDH but also can improve the adsorption of OH^- and reduce the energy barrier for redox reactions. Benefiting from the above optimization, A-CQD/$Co_{0.03}Ni_{0.97}$LDH exhibited a high capacity of 2408 F g^{-1} at 1 A g^{-1} and retained 1665 F g^{-1} at 10 A g^{-1}. In addition, A-CQD/$Co_{0.03}Ni_{0.97}$LDH delivered excellent cycling stability with a capacity retention of 1500 F g^{-1} after 2000 cycles at 10 A g^{-1}. The assembled asymmetric supercapacitors and aqueous Zn–Ni batteries also exhibit excellent electrochemical performance. This work uncovers the CQD-induced mechanism for valence regulation and coordination optimisation in the electrochemical activation process, which provides a novel insight into the performance enhancement mechanism of CQD-modified bimetallic LDH. Moreover, it also provides an inspiration for the design and application of high-performance electrode materials through electrochemical reconstitution.

Author contributions

Wenchao Chen: investigation, data curation, and writing – original draft. Hongying Quan: investigation, data curation, writing – original draft, funding acquisition and supervision. Xiangyu Chen: investigation and data curation. Hua Wang: supervision, writing – reviewing and editing and investigation. Dezhi Chen: conceptualization, supervision, writing – reviewing and editing.

Published on 13 December 2023. Downloaded by Fail Open on 07/05/2025 8:52:43 AM.

Conflicts of interest

There are no conflicts to declare.

Acknowledgements

This work was supported by the National Natural Science Foundation (Grant No. 52063023) of China and the Natural Science Foundation (Grant No. 20202ACBL204012) of Jiangxi Province, China.

References

1 P. Simon, Y. Gogotsi and B. Dunn, Materials Science. Where do Batteries End and Supercapacitors Begin?, *Science*, 2014, **343**, 1210–1211.

2 H. Sun, L. Mei, J. Liang, Z. Zhao, C. Lee, H. Fei, M. Ding, J. Lau, M. Li, C. Wang, X. Xu, G. Hao, B. Papandrea, I. Shakir, B. Dunn, Y. Huang and X. Duan, Three-dimensional holey-graphene/niobia composite architectures for ultrahigh-rate energy storage, *Science*, 2017, **356**, 599–604.

3 C. Wei, Q. Chen, C. Cheng, R. Liu, Q. Zhang and L. Zhang, Mesoporous nickel cobalt manganese sulfide yolk–shell hollow spheres for high-performance electrochemical energy storage, *Inorg. Chem. Front.*, 2019, **6**, 1851–1860.

4 J.-Q. H. Xin-Bing Cheng, H. Yuan, H.-J. Peng, C. Tang, He Liu and Q. Zhang, A perspective on sustainable energy materials for lithium batteries, *SusMat*, 2021, **1**, 38–50.

5 C. Wei, R. Zhang, X. Zheng, Q. Ru, Q. Chen, C. Cui, G. Li and D. Zhang, Hierarchical porous $NiCo_2O_4/CeO_2$ hybrid materials for high performance supercapacitors, *Inorg. Chem. Front.*, 2018, **5**, 3126–3134.

6 Z. Shi, Y. Liu, Y. Zhang, J. Sun, J. Zheng, C. Wei, W. Du, L. Liu and C. Cheng, Designed synthesis of yolk-shelled $NiCo_2O_4/MnCo_2O_4$ hollow sphere with boosted performance for supercapacitors, *Appl. Surf. Sci.*, 2023, **611**, 155758.

7 S. Li, C. Yu, J. Yang, C. Zhao, M. Zhang, H. Huang, Z. Liu, W. Guo and J. Qiu, A superhydrophilic "nanoglue" for stabilizing metal hydroxides onto carbon materials for high-energy and ultralong-life asymmetric supercapacitors, *Energy Environ. Sci.*, 2017, **10**, 1958–1965.

8 J. Yang, C. Yu, C. Hu, M. Wang, S. Li, H. Huang, K. Bustillo, X. Han, C. Zhao, W. Guo, Z. Zeng, H. Zheng and J. Qiu, Surface–confined fabrication of ultrathin nickel cobalt–layered double hydroxide nanosheets for high–performance supercapacitors, *Adv. Funct. Mater.*, 2018, **28**, 1803272.

9 C. Wei, J. Sun, Y. Zhang, Y. Liu, Z. Guo, W. Du, L. Liu and Y. Zhang, Hierarchical $Ni(OH)_2$–MnO_2 hollow spheres as an electrode material for high-performance supercapacitors, *Inorg. Chem. Front.*, 2022, **9**, 3542–3551.

10 C. Chen, S. C. Wang, D. Xiong, M. Gu and F. Y. Yi, Rationally designed trimetallic Prussian blue analogues on LDH/Ni foam for high performance supercapacitors, *Dalton Trans.*, 2020, **49**, 3706–3714.

11 G. Wei, X. Zhao, K. Du, Z. Wang, M. Liu, S. Zhang, S. Wang, J. Zhang and C. An, A general approach to 3D porous CQDs/M_xO_y (M = Co, Ni) for remarkable performance hybrid supercapacitors, *Chem. Eng. J.*, 2017, **326**, 58–67.

12 J. Kang, Y. Xue, J. Yang, Q. Hu, Q. Zhang, L. Gu, A. Selloni, L. M. Liu and L. Guo, Realizing two-electron transfer in Ni$(OH)_2$ nanosheets for energy storage, *J. Am. Chem. Soc.*, 2022, **144**, 8969–8976.

13 C. Deng, J. He, G. Wang, K. Wang, W. Dong and X. Hong, Cyclic voltammetry activation for boosting the supercapacitance of trimetallic Ni-Co-Mn phosphides, *Appl. Surf. Sci.*, 2023, **616**, 156526.

14 J. Peng, W. Zhang, S. Wang, Y. Huang, J. Z. Wang, H. K. Liu, S. X. Dou and S. L. Chou, The emerging electrochemical activation tactic for aqueous energy storage: fundamentals, applications, and future, *Adv. Funct. Mater.*, 2022, **32**, 2111720.

15 S. Li, Y. Zhang, N. Liu, C. Yu, S.-J. Lee, S. Zhou, R. Fu, J. Yang, W. Guo, H. Huang, J.-S. Lee, C. Wang, T. R. Kim, D. Nordlund, P. Pianetta, X. Du, J. Zhao, Y. Liu and J. Qiu, Operando revealing dynamic reconstruction of NiCo carbonate hydroxide for high-rate energy storage, *Joule*, 2020, **4**, 673–687.

16 Q. Li, T. Yang, S. Liao, L. Yang, X. Xu and F. Wang, Insight into the composition effect of nickel cobalt layered double hydroxide nanoarrays with the enhanced synergistic effect for supercapacitor electrode, *J. Energy Storage*, 2022, **50**, 104300.

17 Z. Li, H. Duan, M. Shao, J. Li, D. O'Hare, M. Wei and Z. L. Wang, Ordered-vacancy-induced cation intercalation into layered double hydroxides: a general approach for high-performance supercapacitors, *Chem*, 2018, **4**, 2168–2179.

18 Y. Deng, Z. Liu, A. Wang, D. Sun, Y. Chen, L. Yang, J. Pang, H. Li, H. Li, H. Liu and W. Zhou, Oxygen-incorporated Mo_X (X: S, Se or P) nanosheets via universal and controlled electrochemical anodic activation for enhanced hydrogen evolution activity, *Nano Energy*, 2019, **62**, 338–347.

19 W. Yang, C. Zhang, B. Jiang, P. Wang, L. Yan, L. Hou, F. Yang and Y. Li, Electrochemical activation induced phase and structure reconstruction to reveal cobalt sulfide intrinsic energy storage capacity, *Chem. Eng. J.*, 2022, **434**, 134473.

20 W. Xu, K. Zhao and Y. Wang, Electrochemical activated MoO_2/Mo_2N heterostructured nanobelts as superior zinc rechargeable battery cathode, *Energy Storage Mater.*, 2018, **15**, 374–379.

21 L. Hou, W. Yang, R. Li, X. Xu, P. Wang, B. Deng, F. Yang and Y. Li, Self-reconstruction strategy to synthesis of Ni/Co-OOH nanoflowers decorated with N, S co-doped carbon for high-performance energy storage, *Chem. Eng. J.*, 2020, **396**, 125323.

22 W. Yang, C. Zhang, S. Du, B. Jiang, C. Wang, H. Bai, Z. Li, G. Huang and Y. Li, Potentiostatic Reconstruction of

Published on 13 December 2023. Downloaded by Fail Open on 07/05/2025 8:52:43 AM.

Nickel–Cobalt Hydroxysulfate with Self–Optimized Structure for Enhancing Energy Storage, *Adv. Energy Mater.*, 2022, **12**, 2202286.

23 Q. Pan, P. Hei, Y. Song, J. Meng, C. Liu and X.-X. Liu, Electrochemically activated nickel-cobalt double hydroxide for aqueous ammonium-zinc hybrid battery, *Nano Res.*, 2022, **16**, 2495–2501.

24 P. Zou, L. Yao, C. Wang, S. J. Lee, T. Li and H. L. Xin, Regulating cation interactions for zero-strain and high-voltage P2-type $Na_{2/3}$ $Li_{1/6}$ $Co_{1/6}$ $Mn_{2/3}$ O_2 layered oxide cathodes of sodium-ion batteries, *Angew. Chem., Int. Ed.*, 2023, e202304628, DOI: 10.1002/anie.202304628.

25 X. Li, H. Wu, C. Guan, A. M. Elshahawy, Y. Dong, S. J. Pennycook and J. Wang, (Ni,Co)Se_2/NiCo-LDH core/shell structural electrode with the cactus-like (Ni,Co)Se_2 core for asymmetric supercapacitors, *Small*, 2019, **15**, e1803895.

26 F. Lu, Y. Ji, D. Shi, J. Yao and L. Pei, Electrochemically activated 3D Mn doped NiCo hydroxide electrode materials toward high-performance supercapacitors, *J. Colloid Interface Sci.*, 2023, **641**, 510–520.

27 X. Hong, C. Deng, G. Wang, X. Wang and W. Dong, Composition and morphology transition of NF/MnP/NiCoP composite electrode induced by charge/discharge activation, *Chem. Eng. J.*, 2023, **451**, 139036.

28 M. Cui, X. Bai, J. Zhu, C. Han, Y. Huang, L. Kang, C. Zhi and H. Li, Electrochemically induced $NiCoSe_2$@NiOOH/CoOOH heterostructures as multifunctional cathode materials for flexible hybrid zn batteries, *Energy Storage Mater.*, 2021, **36**, 427–434.

29 P. Zhang, J. S. Wei, X. B. Chen and H. M. Xiong, Heteroatom-doped carbon dots based catalysts for oxygen reduction reactions, *J. Colloid Interface Sci.*, 2019, **537**, 716–724.

30 H. Quan, W. Zeng, W. Chen, Y. Wang, W. Tao and D. Chen, Carbon quantum dot-induced robust ε-MnO_2 electrode by synergistic engineering of oxygen vacancy and low crystallinity for high-performance flexible asymmetric supercapacitor, *J. Alloys Compd.*, 2023, **938**, 168524.

31 W. Chen, H. Quan and D. Chen, Carbon quantum dots boosted structure stability of nickel cobalt layered double hydroxides nanosheets electrodeposited on carbon cloth for energy storage, *Surf. Interfaces*, 2023, **36**, 102498.

32 W. Luo, W. Chen, H. Quan, Z.-X. Zhang, Y. Zeng, Y. Wang and D. Chen, Strongly coupled carbon quantum dots/NiCo-LDHs nanosheets on carbon cloth as electrode for high performance flexible supercapacitors, *Appl. Surf. Sci.*, 2022, **591**, 153161.

33 H. Jiang, K. Tian, H. Pang and Y. Hao, Enhanced photocatalytic degradation of bisphenol A over N,S-doped carbon quantum dot-modified MIL-101(Fe) heterostructure composites under visible light irradiation by persulfate, *Appl. Surf. Sci.*, 2021, **577**, 151902.

34 B. Ravel and M. Newville, ATHENA, ARTEMIS, HEPHAESTUS: data analysis for X-ray absorption spectroscopy using IFEFFIT, *J. Synchrotron Radiat.*, 2005, **12**, 537–541.

35 G. Zhang, J. Hu, Y. Nie, Y. Zhao, L. Wang, Y. Li, H. Liu, L. Tang, X. Zhang, D. Li, L. Sun and H. Duan, Integrating Flexible Ultralight 3D Ni Micromesh Current Collector with NiCo Bimetallic Hydroxide for Smart Hybrid Supercapacitors, *Adv. Funct. Mater.*, 2021, **31**, 2100290.

36 C.-Y. Chiu, Y. Li and Y. Huang, Size-controlled synthesis of Pd nanocrystals using a specific multifunctional peptide, *Nanoscale*, 2010, **2**, 927–930.

37 Y. Yu, Q. Zhang, X. Lu and J. Y. Lee, Seed-mediated synthesis of monodisperse concave trisoctahedral gold nanocrystals with controllable sizes, *J. Phys. Chem. C*, 2010, **114**(25), 11119–11126.

38 F. Kim, K. Sohn, J. Wu and J. Huang, Chemical synthesis of gold nanowires in acidic solutions, *J. Am. Chem. Soc.*, 2008, **130**, 14442–14443.

39 C. Cheng, B. Liu, H. Yang, W. Zhou, L. Sun, R. Chen, S. F. Yu, J. Zhang, H. Gong, H. Sun and H. J. Fan, Hierarchical assembly of ZnO nanostructures on SnO_2 backbone nanowires: low-temperature hydrothermal preparation and optical properties, *ACS Nano*, 2009, **3**(10), 3069–3076.

40 Y. Xuemin, L. Hejun, Y. Ruimei and L. Jinhua, NiCoLDH nanosheets grown on MOF-derived Co_3O_4 triangle nanosheet arrays for high-performance supercapacitor, *J. Mater. Sci. Technol.*, 2021, **62**, 60–69.

41 H. Gao, H. Yang, J. Xu, S. Zhang and J. Li, Strongly coupled g-C_3N_4 nanosheets-Co_3O_4 quantum dots as 2D/0D heterostructure composite for peroxymonosulfate activation, *Small*, 2018, e1801353.

42 L. Malfatti, P. Falcaro, D. Marongiu, M. F. Casula, H. Amenitsch and P. Innocenzi, Self-Assembly of shape controlled hierarchical porous thin films: mesopores and nanoboxes, *Chem. Mater.*, 2009, **21**(20), 4846–4850.

43 X. Hong, X. Wang, J. Fu, Y. Li and B. Liang, Spreading GO nanosheets-coated nickel foam decorated by $NiCo_2O_4$/$NiCo_2S_4$ nanoarrays for high-performance supercapacitor electrodes, *Electrochim. Acta*, 2021, **385**, 138437.

44 Y. Dong, C. Chen, J. Lin, N. Zhou, Y. Chi and G. Chen, Electrochemiluminescence emission from carbon quantum dot-sulfite coreactant system, *Carbon*, 2013, **56**, 12–17.

45 B. Sun, M. Vafaie, L. Levina, M. Wei, Y. Dong, Y. Gao, H. T. Kung, M. Biondi, A. H. Proppe, B. Chen, M. J. Choi, L. K. Sagar, O. Voznyy, S. O. Kelley, F. Laquai, Z. H. Lu, S. Hoogland, F. P. Garcia de Arquer and E. H. Sargent, Ligand-Assisted reconstruction of colloidal quantum dots decreases trap state density, *Nano Lett.*, 2020, **20**, 3694–3702.

46 Z. Zhang, L. Wang, S. Lou, L. Xiang, B. Xie, Q. Wang, C. Du, J. Wang and G. Yin, Stacking fault disorder induced by Mn doping in $Ni(OH)_2$ for supercapacitor electrodes, *Chem. Eng. J.*, 2021, **412**, 128617.

47 T. Liang, R. Hou, X. Zhang, B. Yang, B. Yang, S. Yang, X. Zhang and X. Yan, Spintronic state-induced interface reconfiguration of 2H-perovskite related oxides for pseudocapacitance increase, *Adv. Funct. Mater.*, 2023, **33**, 2302272.

Published on 13 December 2023. Downloaded by Fail Open on 07/05/2025 8:52:43 AM.

48 B. Liu, X. Wang, S. Wang, H.-Q. Peng, T. Xiao, G. Liu, S. Bai, Y. Zhao, W. Zhang and Y.-F. Song, Hydroxyl vacancies triggered high methanol oxidation activity of monolayered layered double hydroxides for energy-saving hydrogen production, *Mater. Today Energy*, 2022, **28**, 101082.

49 N. Li, C. Zhu, J. Zhang, H. Jing, J. Hu, C. Hao and Y. Shi, Single-atom-catalyst with abundant Co-S_4 sites for use as a counter electrode in photovoltaics, *Chem. Commun.*, 2021, **57**, 5302–5305.

50 Y. Duan, J. Y. Lee, S. Xi, Y. Sun, J. Ge, S. J. H. Ong, Y. Chen, S. Dou, F. Meng, C. Diao, A. C. Fisher, X. Wang, G. G. Scherer, A. Grimaud and Z. J. Xu, Anodic oxidation enabled cation leaching for promoting surface reconstruction in water oxidation, *Angew. Chem., Int. Ed.*, 2021, **60**, 7418–7425.

51 Y. Tang, H. Shen, J. Cheng, Z. Liang, C. Qu, H. Tabassum and R. Zou, Fabrication of oxygen–vacancy abundant NiMn–layered double hydroxides for ultrahigh capacity supercapacitors, *Adv. Funct. Mater.*, 2020, **30**, 201908223.

52 Y. X. Bang Lan, X. Luo, D. Wu, L. Zhang, J. Duan, M. Guo, Y. Ito and Y. Liu, Charge regulation engineering to suppress Jahn-Teller distortion in low crystallinity In-doping $MnCo_2O_4$ for high activity pseudocapacitors and hydrogen evolution reaction, *Chem. Eng. J.*, 2021, **430**, 132886.

53 T. Deng, W. Zhang, O. Arcelus, J. G. Kim, J. Carrasco, S. J. Yoo, W. Zheng, J. Wang, H. Tian, H. Zhang, X. Cui and T. Rojo, Atomic-level energy storage mechanism of cobalt hydroxide electrode for pseudocapacitors, *Nat. Commun.*, 2017, **8**, 15194.

54 X. W. Lou, L. A. Archer and Z. Yang, Hollow micro-nanostructures: synthesis and applications, *Adv. Mater.*, 2008, **20**, 3987–4019.

55 X. Pu, D. Zhao, C. Fu, Z. Chen, S. Cao, C. Wang and Y. Cao, Understanding and calibration of charge storage mechanism in cyclic voltammetry curves, *Angew. Chem., Int. Ed.*, 2021, **60**, 21310–21318.

56 J. Lin, E. Fan, X. Zhang, Z. Li, Y. Dai, R. Chen, F. Wu and L. Li, Sustainable upcycling of spent lithium–ion batteries cathode materials: stabilization by in situ Li/Mn disorder, *Adv. Energy Mater.*, 2022, **12**, 2201174.

57 C. M. Cobley, M. Rycenga, F. Zhou, Z.-Y. Li and Y. Xia, Controlled etching as a route to high quality silver nanospheres for optical studies, *J. Phys. Chem. C*, 2009, **113**, 16975–16982.